Volume 18
Number 46
14 December 2022
Pages 8705–8910

Soft Matter

rsc.li/soft-matter-journal

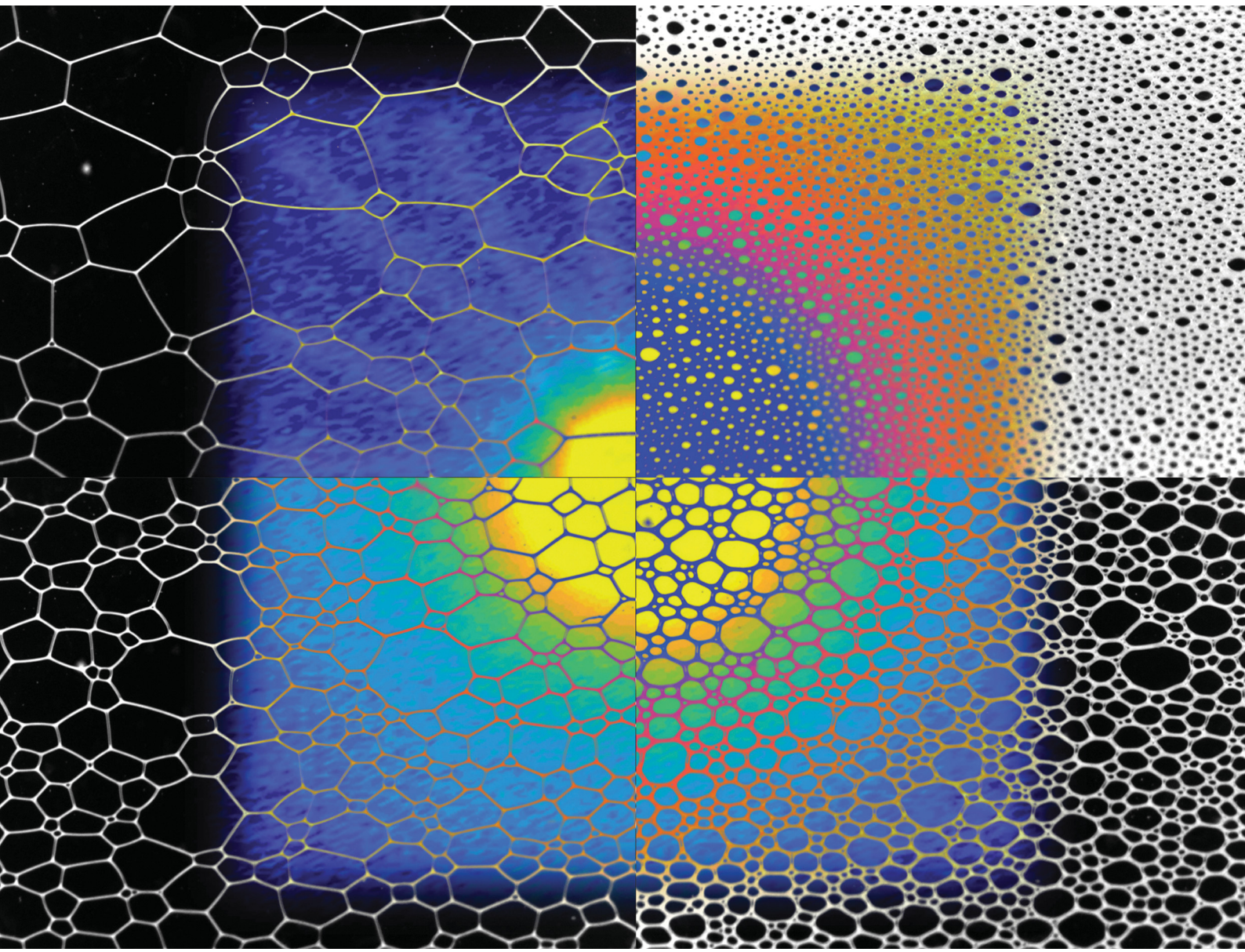

ISSN 1744-6848

ROYAL SOCIETY OF CHEMISTRY

PAPER

Leonardo Chiappisi *et al.*
Probing foams from the nanometer to the millimeter scale by coupling small-angle neutron scattering, imaging, and electrical conductivity measurements

Soft Matter

PAPER

View Article Online
View Journal | View Issue

Cite this: *Soft Matter*, 2022, 18, 8733

Probing foams from the nanometer to the millimeter scale by coupling small-angle neutron scattering, imaging, and electrical conductivity measurements†

Julien Lamolinairie,[a] Benjamin Dollet,[b] Jean-Luc Bridot,[c] Pierre Bauduin,[d] Olivier Diat[d] and Leonardo Chiappisi *[a]

Liquid foams are multi-scale structures whose structural characterization requires the combination of very different techniques. This inherently complex task is made more difficult by the fact that foams are also intrinsically unstable systems and that their properties are highly dependent on the production protocol and sample container. To tackle these issues, a new device has been developed that enables the simultaneous time-resolved investigation of foams by small-angle neutron scattering (SANS), electrical conductivity, and bubbles imaging. This device allows the characterization of the foam and its aging from nanometer up to centimeter scale in a single experiment. A specific SANS model was developed to quantitatively adjust the scattering intensity from the dry foam. Structural features such as the liquid fraction, specific surface area of the Plateau borders and inter-bubble films, and thin film thickness were deduced from this analysis, and some of these values were compared with values extracted from the other applied techniques. This approach has been applied to a surfactant-stabilized liquid foam under free drainage and the underlying foam destabilization mechanisms were discussed with unprecedented detail. For example, the information extracted from the image analysis and SANS data allows for the first time to determine the disjoining pressure *vs.* thickness isotherm in a real, draining foam.

Received 14th September 2022,
Accepted 28th October 2022

DOI: 10.1039/d2sm01252a

rsc.li/soft-matter-journal

1 Introduction

Liquid foam structure and aging are influenced by several physical and chemical parameters, such as the type of gas,[1,2] the surfactant used,[3,4] the liquid fraction,[5–7] the size of bubbles,[8,9] the thickness of the inter-bubble film,[10–12] the surface tension[13,14] and the interfacial elastic modulus.[15,16] Predicting the dominant factors to control the resulting foam properties is therefore a challenging task. For example, how the texture and taste of beer depend on the foam structure – notably on size and number of bubbles – has only recently been understood.[17,18] Even the surface state of the container plays a role and can contribute to a rapid breakdown of the foam. To further develop on the example of beverages, superamphiphobic surface coatings are used to prevent the formation of unwanted foam during the filling of bottles.[19] Foams are not limited to beverages, and can be found in many other applications: detergency, food, cosmetics, and also for industrial processes such as froth or foam flotation applied for materials or waste recycling, oil recovery from the ground, fire-fighting, mitigation of blast waves from explosions with very active research in each of these fields nowadays.[20–25] Depending on the application, the desired foam properties might vary considerably. Sometimes, an expanded and stable foam is required, for example in firefighting applications, to create a dense blanket acting as an insulating barrier between the fuel and the air and preventing the development of combustion.[26] Sometimes, as for cleaning, a rather unstable foam shows better performance.[27]

However, the importance of each of the parameters listed above and more especially their coupled influences on the structural evolution of foams remain difficult to quantify because foams are multi-scale structures. The different structural scales of the foam are depicted in Fig. 1 and can be probed using suitable techniques. At the centimetre scale, optical studies provide general information on the foamability, *i.e.* the amount of gas that can be trapped in foam. It is also possible to measure the size distribution of gas bubbles[28,29] that create in close contact, when the foam dries, a continuous network of

[a] *Institut Max von Laue – Paul Langevin (ILL), 71 Avenue des Martyrs, 38042 Grenoble, France. E-mail: chiappisil@ill.fr*
[b] *Université Grenoble Alpes, CNRS, LIPhy, 38000 Grenoble, France*
[c] *Teclis Scientific, 69380 Civrieux-d'Azergues, France*
[d] *ICSM, Univ Montpellier, CEA, CNRS, ENSCM, Marcoule, France*

† Electronic supplementary information (ESI) available. See DOI: https://doi.org/10.1039/d2sm01252a

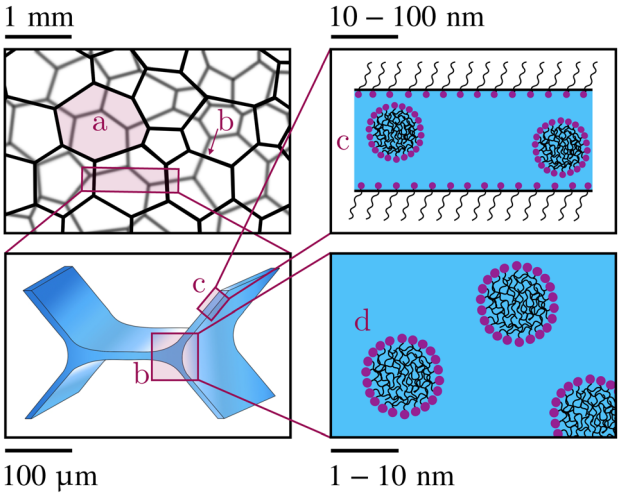

Fig. 1 Schematic representation of a liquid foam at different length scales from millimeter to nanometer. The different elements of a foam are identified by a letter: (a) a bubble, (b) a Plateau border, (c) a film/lamella and (d) a micelle.

liquid channels (Plateau borders) connected by nodes and thin films. At the bubble scale (>100 µm), this 3D network evolution and connectivity can be understood through foam rheology analysis.[30,31] Foam drainage is primarily governed by the vertical flow of the liquid due to gravity through these channels and nodes and strongly depends on the viscosity of the fluid.[32,33] Then, inter-bubble films, stabilized at both interfaces by surfactants or other colloidal particles, start to thin which initiates or accelerates phenomena of bubble ripening and/or coalescence. Depending on the cohesive interactions between surfactant molecules at water/air interfaces and their dynamic exchange between interfaces and the bulk solution, foam aging can be slowed down or accelerated. Repulsive interactions between facing surfactant monolayers, of electrostatic or steric origin, can also be tuned to counterbalance the capillary pressure that increases as the Plateau borders become thinner and more curved.[34] It is through the succession of film ruptures that the foam collapses. Accordingly, information on the film thickness (<100 nm), correlated to that at other scales, is crucial for a deep understanding of the stability of the foam. The stability of the foam might further be impacted by the presence of colloidal aggregates (1–10 nm), such as surfactant micelles or proteins.[35,36]

Commercial foam analyzers are recurrently used to study foams. They allow liquid foams to be generated by mechanical means – beating or whipping the solution – or by bubbling gases through porous plates. Once generated, various structural foam parameters, such as water volume fraction, foam height, and bubble size distribution are followed over time by image processing and electrical techniques. This information, although crucial to probe the foam destabilization mechanism, lacks an essential piece of information: the inter-bubble film thickness. A common method to measure it is the thin film pressure balance. A surfactant film is subjected to external gas pressure and the difference with the capillary pressure causes the film to drain until the pressures are balanced.[37,38] The film thickness is then measured by interferometry as a function of the applied pressure to build a pressure isotherm allowing the experimentalist to quantify the interactions between facing interfaces. However, these experiments are carried out on isolated films, and the extrapolation of these observations to the evolution of the 3D structures such as liquid foams where other effects impact the drainage is far from trivial.

In situ foam film thickness measurement is possible performing small-angle neutron scattering (SANS).[39–48] SANS data also provide information on the internal structure of the foam solution over a large length scale. The relatively large diameter of the beam (a few tens of millimetres) allows the probing of several hundred bubbles and films. This method, therefore, provides acceptable statistics on data collected during time scales of a few minutes, a sufficient temporal resolution if the foam does not collapse too quickly. The first cell was manufactured in the early 2000 s and consisted of a Plexiglas cell with a quartz window allowing the study of foam at a single given height.[49] Since then, interest in this technique has continued to grow with new cells recently developed.[50] The technique has been employed to investigate stimuli responsive foams,[42,43] foams stabilized by polymeric surfactants,[44] proteins,[45] or, more recently, nano-ions.[47]

While SANS enables us to determine with precision the thickness of films in real foams, it is essential to characterize the foam in its entirety and on all its scales simultaneously: from the bubble to the film, in order to optimize the different parameters involved in the aging of the foam. To address this challenge, we have developed a new device that enables to simultaneously collect microscopic information on the foam *via* SANS experiments and macroscopic information, with the acquisition of 2D images using an optical camera, as well as conductivity data measured through the foam. Moreover, we have developed an analysis framework to combine the results obtained simultaneously from the different techniques.

In this article, we present the features of this new device as well as the methodology for data analysis. The possibilities offered by the combined analysis are demonstrated using a foam stabilized by a commercial non-ionic polyoxyethylene (10) oleyl ether surfactant (BrijO10) with a very low CMC[51] and good foaming capacity,[52] and with the anionic sodium dodecyl sulfate (SDS) to induce an electrostatic stabilization of the foam.

2 Materials and methods

2.1 Materials

The non-ionic surfactant polyoxyethylene (10) oleyl ether surfactant BrijO10 ($C_{18:1}E_{10}$) and the ionic surfactant sodium dodecyl sulfate (SDS, $NaC_{12}H_{25}SO_4$, ≥99.0%) were purchased from Sigma Aldrich and were used without further purification. The data presented in this article were conducted with a foam stabilized with 0.5 mM BrijO10 which is well above the critical micelle concentration of 40 µM molar[51] and upon addition of 0.2 mM SDS. Samples were prepared in Millipore water for

Foam-analyser experiments and in D_2O purchased from Eurisotop (99.9% isotopic purity) for small-angle neutron scattering (SANS) experiments.

2.2 Quartz column

The main part of the new device is a column – entirely made of quartz, a material transparent for neutrons – and designed on the model of the FOAMSCAN from Teclis Scientific (France) in which the foam is formed. This cell, shown in Fig. 2a and b, is cylindrical (30 cm high with an internal diameter of 3.5 cm and a wall thickness of 2 mm) and is always opened at the top. A flat face was machined to glue four prisms at different fixed heights, allowing image capture of the bubbles in contact with the wall. Five pairs of electrodes were also integrated to measure the conductance through the foam at different heights. This cell is therefore compatible with the FOAMSCAN and can be used both in a laboratory and on a neutron diffractometer dedicated to small-angle scattering technique.

The quartz cell is clipped onto a base *via* an O-ring to get a set "column and rigid support" tight but easy to dismount for efficient cleaning. The base is composed of a silica frit (pore size 10–16 μm, porosity P16 (ISO 4793)) and can be exchanged depending on the required bubbling size. The flux of injected gas is controlled by a digital Mass Flow Controller (MFC) from MKS Instruments (Andover, Massachusetts, U.S.) with a flow range 0–100 mL min^{-1} for model GE50 series. When the foaming solution is injected into the bottom of the column, a slight overpressure is maintained to avoid filling the pores of the frit with the solution (with a gas flow rate of 2 mL min^{-1}). The foams are then produced with a gas flow rate of 50 mL min^{-1} using nitrogen. On the diffractometer, the cell was fixed on a set of *X*–*Z* stages (as shown in Fig. 2c) to first center the cylinder in the neutron beam path and second to vary its *Y*-position so that the neutron beam passes through the cell at heights predefined by the position of the prisms and to be able to simultaneously capture photographs of the foam probed by neutrons.

2.3 Image capture

The photographs of the foam were taken with the acA780-75gm camera from BASLER (Germany). It consists of a Sony ICX415AL CCD sensor with a diagonal of 8 mm and a resolution of 782 × 582 pixels. A Computar TEC-M55 55 mm Telecentric Lens (C Mount) with a focal length of 55 mm and an F11 aperture is added to provide a sharp image at a minimum distance of 14 cm. The telecentric lens also allows only light rays parallel to the optical axis to be selected. The light source and camera are located on either side of the prism, at an angle of 45° to the column wall. This experimental method allows us to visualize only the layer of bubbles located against the inner wall of the column. In the images, the bubbles appear white and the dark part corresponds to the Plateau borders.[53] The scaling calibration is done with a calibrated steel ball, 2 mm, fixed in mobile support that can be placed in front of the prism before starting the photographic captures.

2.4 Conductance measurements

Electronic conductivity measurements were performed using an EPU 452 Quad Multi-Function isoPod developed by eDAQ (Colorado Springs, CO, US) and configured to measure ionic conductance $G = k\sigma$. The cell-constant k in cm only depends on the distance between the electrodes and the surface area of the

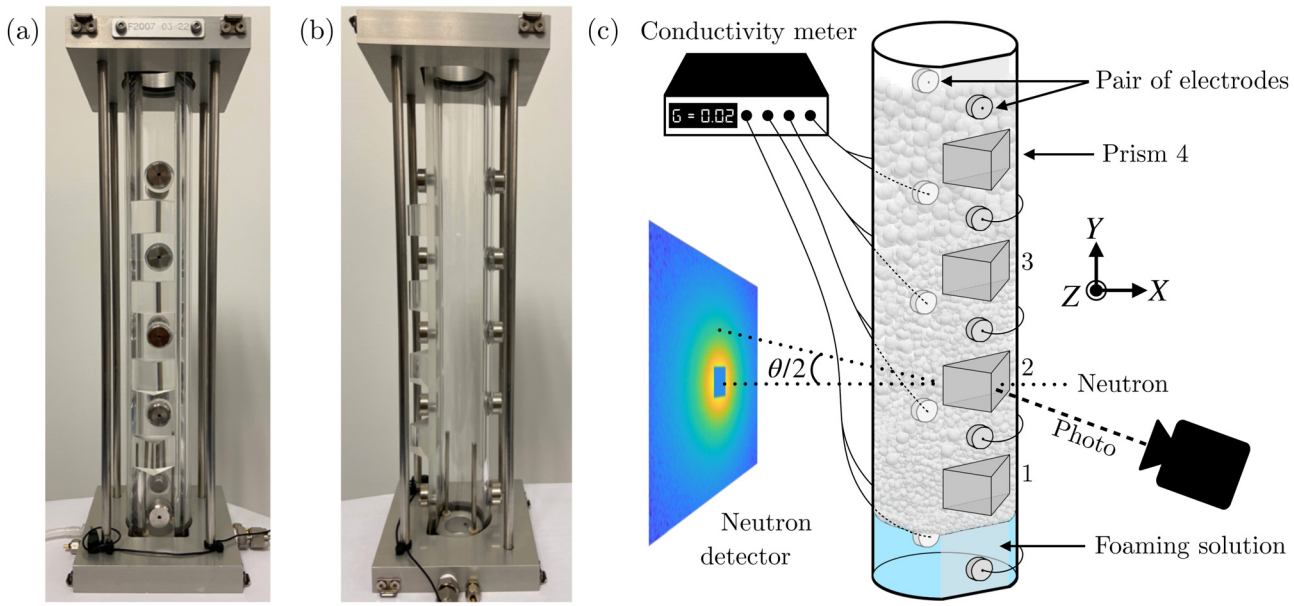

Fig. 2 (a) Photograph of the quartz cell in front view and (b) rotated by 90°. (c) Schematic representation of the developed multi-scale device which enables the simultaneous characterization of the foam *via* the measurement of the conductance *G* through the foaming solution and the foam, the imaging of the foam on the 2nd prism and the measurement of the neutron scattering curves at the 2nd prism height. The cell can be translated in *Y* direction to probe the foam at different heights.

electrodes, which are equivalent for each position of the pair of electrodes. The cell constants of the different electrodes were calibrated using dilute NaCl solutions.

2.5 Small-angle neutron scattering (SANS)

Small-angle neutron scattering (SANS) experiments were performed at room temperature on the D33 diffractometer[54] at Laue-Langevin Institute (ILL) in Grenoble. We opted for the monochromatic mode with a wavelength λ = 6 Å. The detector consists of a central panel set at 10 m and 4 side panels set at 1.7 m. The collimation length was set to 12.8 m and the beam size at the sample position was fixed at 15 mm in diameter. Under these conditions, the accessible scattering vector **q** range, with q defined as $q = 4\pi\sin(\theta/2)/\lambda$, varies from 0.002–0.25 Å. The neutron beam was set at the same height as the camera to correlate the various collected data. Acquisition time was fixed at 60 s for scattering data and 30 s for transmission data. Normalization and azimuthal averaging of the 2D data were applied using the GRASP software package.[55] The empty cell signal was subtracted for each scattering curve. The absolute scale was obtained by normalizing the neutron beam flux. The experiments described in this article were performed at the height of the second prism, at 8 cm above the level of the solution at rest. SANS experiments were also conducted on foaming solutions in a quartz cuvette of 2 mm thick on the D22 diffractometer to obtain structural information of micellar solution. In this configuration, neutron wavelength was also set at 6 Å and with two detector distances at 1.4 and 17.6 m and with a 17.6 m collimation, resulting in a **q**-vector range from 0.003 to 0.64 $Å^{-1}$.

The SANS data analysis was performed in absolute units, considering the scattering length densities and molecular volumes given in Table S1 in the ESI.† The models are described later in the text. The best-fitting parameters and their uncertainty were estimated by least-square minimization.

2.6 Foam generation and aging procedure

Before SANS measurements, foams were studied using the FOAMSCAN apparatus by injecting 40 mL of the foaming solution into the column in 10 mL steps through the inlet at the bottom of the column, just above the frit. After each injection step, the conductance was measured, resulting in a linear calibration curve (conductance *versus* liquid volume). Then, N_2 flowed at 50 mL min^{-1} through the porous frit. Once the column was filled by the foam, the N_2 flow was stopped leaving the foam under free drainage conditions for 2 to 3 hours. The foam structure was captured using one camera when using the FOAMSCAN. The sample was analyzed 3 times from a fresh foaming solution. The quartz column was rinsed generously with Millipore water and dried after each test. The SANS experiments were performed using the same procedure: after stopping the gas flux, the evolution of the foam was followed using simultaneously conductivity, imaging, and SANS techniques for 75 minutes (see Fig. 2c).

2.7 Surface tension measurement

The surface tension of the surfactants at the air–water interface was measured at room temperature using a Tracker developed by Teclis Scientific. The measurement of surface tension was performed on bubbles of 5 μL for 10 min. This measurement was repeated 3 times and the surface tension obtained is $\gamma = (32 \pm 1)$ mN m^{-1}.

3 Data analysis procedure

3.1 Data collection

The foam is generated in the quartz cell from the foaming solution containing the nonionic surfactant Polyoxyethylene (10) oleyl ether (Brij O10) at 0.5 mM doped with 0.2 mM sodium dodecyl sulfate. The molar ratio of anionic to nonionic surfactant is 1/2.5. The gas flow is stopped once the column is filled, defining the starting point t = 0 of the time-resolved experiments. The structure of the foam is then investigated as a function of time at the level of prism 2 for this study, at approx. 8 cm above the liquid surface, as shown in Fig. 2c. The measurement of the conductance was performed simultaneously through the foaming solution and the foam at three different heights. Fig. 3 presents a typical set of kinetics data recorded simultaneously during the free drainage of a foam: 2D SANS scattering data (Fig. 3a and c) with the corresponding radially averaged scattering curves (Fig. 3f), 2D optical images of the foam (Fig. 3b and d), and conductance values recorded on electrode pairs below and above the prism 2 (Fig. 3e).

3.2 Image processing

The collected optical images were binarised to extract the relevant information: bubble size, liquid volume fraction, specific surface area of the foam, and radius of the Plateau borders. This binarisation process was automated using the "Adaptive Threshold" command from OpenCV package,[56] for which the binarisation threshold value varies for each pixel depending on the gray level of its neighborhood. Once the image is binarised, "findContours" and "drawContours" commands from OpenCV package[56] are applied to remove artefacts from impurities within the bubbles. The source code used for the image treatment is provided in Section S2 of the ESI.† An updated version of the software is freely available at **https://github.com/leonardo-chiappisi/pyFoam_analysis**.

From the binarised images, the surface area of each bubble in contact with the wall of the column S_{bubble} was measured as well as their surface radius expressed as $r = \sqrt{S_{bubble}/\pi}$. The distribution of the radii can be characterized by the Polydispersity Index (PI) expressed as

$$PI = \frac{\sqrt{\langle r^2\rangle - \langle r\rangle^2}}{\langle r\rangle}. \quad (1)$$

If PI is greater than 0.2, it was demonstrated through simulations that the distributions of the surface radii are well correlated with those of the 3D bubbles.[57] Since for the investigated system we found PI > 0.37, we no longer distinguish between the surface radius and volume radius.

From the foam images, the liquid fraction ϕ is also determined as a function of time. Its estimation is based on the

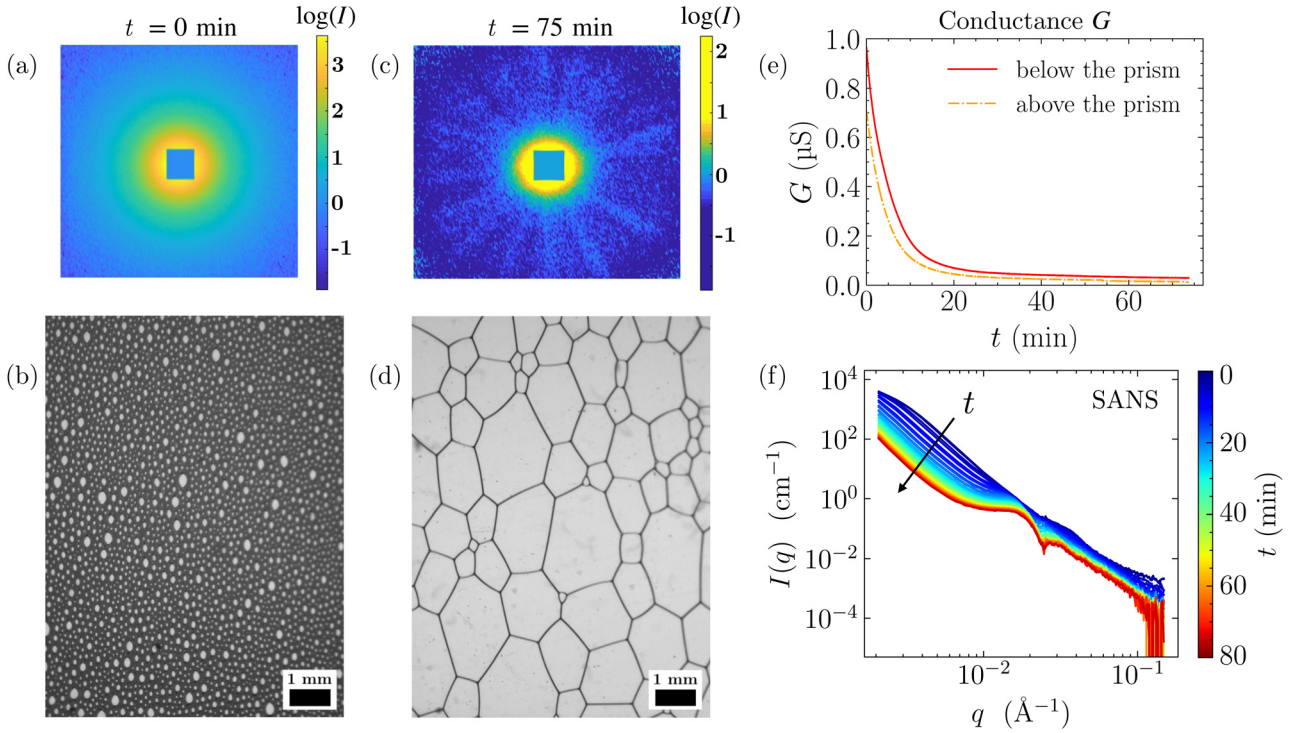

Fig. 3 Classic set of experimental data with an example of 2D SANS data on the central detector (a and c) at the beginning and the end of the experiment respectively and corresponding photographs of the foam taken at the level of prism 2 (b and d). (e) Time dependence of the conductance G measured on the pair of electrodes below and above prism 2. (f) Radially averaged SANS data as a function of time from blue, t = 0 min to red, t = 75 min. The arrow is in the direction of increasing time.

calculation of the surface fraction ϕ_s, expressed as the ratio between the area of the pseudo Plateau borders A_{PB} – that corresponds to the number of black pixels after binarization – and the total area of the foam A_{foam}: $\phi_s = A_{PB}/A_{foam}$. By considering the foam as a network of liquid channels with a characteristic length close to the bubble radius, a relationship exists between ϕ_s and ϕ using the following equation:[58]

$$1 - \phi_s = \left(1 - \sqrt{\frac{\phi}{\phi_c}}\right)^2 \quad (2)$$

where ϕ_c is the critical liquid fraction, which is close to 0.36 in the case of a polydisperse foam.[58] An uncertainty on these data can be determined by taking into account that the threshold value chosen for the binarization will modify the number of black pixels and thus the value of the liquid fraction. To estimate the dispersity of this value, different threshold values were tested.

The specific surface area of the foam, *i.e.* the ratio of the total surface area of the water/air interfaces over the total volume of foam, can also be estimated by image analysis. The model holds for dry polydispersed foams, where the surface size distribution obtained from the images represents the true bulk polydispersity of the foam. In this case, the specific surface area of the foam can be approximated by:

$$\left.\frac{S}{V}\right|_{img} \simeq \frac{l_{PB}}{S_{photo}} = \frac{N_{black}}{N_{total} \times l_{1px}} \quad (3)$$

with l_{PB} the total length of all Plateau borders in the picture, S_{photo} the area of the picture. After applying a topological skeleton process to reduce Plateau borders to single-pixel-wide shapes (see Section S2 in the ESI† for more information), the specific surface is equal to the ratio between the number of black pixels N_{black} and the number of pixels of the image N_{total} multiplied by the side-length of one pixel $l_{1px} = 1.2 \times 10^{-3}$ cm. The uncertainty of the data is obtained by applying the same skeletonization procedure but using a different image processing program, ImageJ.

It is also possible to extract the radius of the Plateau borders r_{PB} from the binarised and skeletonized images. The analysis method is detailed in Section S2 of the ESI.†

3.3 Conductance data

The liquid fraction ϕ is also determined using electrical conductance values. This measurements is possible for the investigated system thanks to the presence of a charged surfactant. The following empirical relation is valid for both wet and dry foams:[59]

$$\phi = \frac{3\sigma_r(1 + 11\sigma_r)}{1 + 25\sigma_r + 10\sigma_r^2} \quad (4)$$

with $\sigma_r = \sigma_{foam}/\sigma_{liquid}$ the ratio between the measured conductivity through the foam and the liquid. The ratio of conductivities σ_r can be approximated by the ratio of conductances $G_r = G_{foam}/G_{liquid} = k\sigma_{foam}/k\sigma_{liquid} = \sigma_r$ since the constant cell k is

similar at all heights of the cell. For the BrijO10 + SDS solution, the conductance measured at the bottom of the cell is equal to G_{liquid} = 10.5 μS. As can be seen in Fig. 3e, since the electrodes are located below and above the prism, the conductivities are averaged to provide the value of ϕ at the height of the neutron beam. It is possible to determine the maximum error made on the liquid fraction measurement using the sensitivity of the conductivity meter – for the 2 μS range used, the error is lower than 1% full scale – which is then propagated to obtain the maximal error on ϕ.

3.4 SANS data analysis

A third approach was followed to study the liquid volume fraction evolution by applying the Beer–Lambert law from the neutron transmission values and using 1.549 cm as adsorption length for D_2O.[60] The uncertainty on the transmission ΔT related to the counting statistic of the 2D detector is propagated to obtain the uncertainty on the liquid fraction. The transmission value measured at 6 min is equal to 0.85 and is higher than 0.99 after 17 min. The values are high enough to safely neglect multiple scattering.

In addition to the determination of the liquid fraction of the foam, small-angle scattering is mainly employed for the microstructural characterization of the foam. In particular, given the large size of the neutron beam (15 mm diameter), the large sample thickness (3.5 cm), and the relatively small size of the bubbles (~1 mm), isotropic scattering patterns are obtained throughout the drainage, except at the end of the sequence when the foam is very dry. Given the fact that the characteristic sizes associated with the different contributions strongly differ – a few nm for the micelles, a few tens of nanometers for the films, several μm for the Plateau borders – the azimuthal averaged SANS intensities can be analyzed as the coherent sum of different contributions.

3.4.1 Contribution of micelles. When working above the critical micelle concentration (CMC) of the surfactant, micellar aggregates are present in the solution, as well as in the liquid within the foam. Herein, we assume that the size, shape, and concentration of micelles within the Plateau borders are equal to the measured parameters of the micelles in the foaming solution. This assumption is required to reduce the number of unknown parameters during the analysis procedure and will be discussed in Section 4.2. The foaming solution was thus investigated separately to determine the micellar structural parameters and the intermicellar interactions used to compute the scattering form and structure factors, respectively. A model of core–shell ellipsoidal micelles interacting *via* a charged hard-sphere potential was used. Full details are provided in Section S3 in the ESI.† The contribution of the micelle scattering is described as:

$$I_{micelle}(q) = {}^1N \cdot \phi \cdot P_{CS}(q) S_{cHS}(q) \quad (5)$$

with ${}^1N$ the particle number density in solution, ϕ the liquid fraction in the foam, $P_{CS}(q)$ the scattering form factor and S_{cHS} the scattering structure factor (see ESI†). Under the aforementioned assumptions, only the liquid fraction ϕ of the solution within the foam remains an adjustable parameter and will be compared and discussed with the liquid volume fractions determined using the other complementary analysis.

3.4.2 Contribution of Plateau borders (PB). At q values below 5×10^{-3} Å^{-1}, a scattering intensity decay close to q^{-4} power law is clearly visible for both wet and dry foams. The q^{-4} signal in SANS is characteristic of well-defined interfaces scattering and is described by the Porod law.[61] These interfaces of characteristic size $d \gg 0.125$ μm can be associated to the network of Plateau borders. The scattering intensity applied to air–D_2O system is expressed as:

$$I_{PB}(q) = 2\pi\Delta\rho^2 \frac{S}{V}\bigg|_{PB} \frac{1}{q^4} \quad (6)$$

where $S/V|_{PB}$ the specific surface area of the Plateau borders and $\Delta\rho^2$ the difference in scattering length density of D_2O and air.

3.4.3 Contribution of lamellae. Films between adjacent bubbles are another major structural component of foams. For sufficiently dry foams, the foam bubbles are polyhedral.[62] For the sake of simplicity, to calculate the contribution of the scattering from the foam lamellae, the system is modeled as a collection of randomly oriented large discs of radius r. A schematic representation is given in Fig. 4a. Hereafter, two approaches to compute the scattering intensity are presented.

In the first approach, the contribution of the foam films is calculated considering scattering from flat discs of radius r and thickness h, *i.e.*, with $h \ll r$:[63]

$$I^{scatt}_{lamellae}(q) = 8^1 N_{tot} \Delta\rho^2 \frac{(\pi r^2 h)^2}{(qr)^2} \frac{1 - J_1(2qr)}{qr} \frac{\sin^2\left(\frac{qh}{2}\right)}{(qh)^2} \quad (7)$$

where J_1 is the first-order Bessel function, and the scattering contrast $\Delta\rho$ is the difference in scattering length density of D_2O

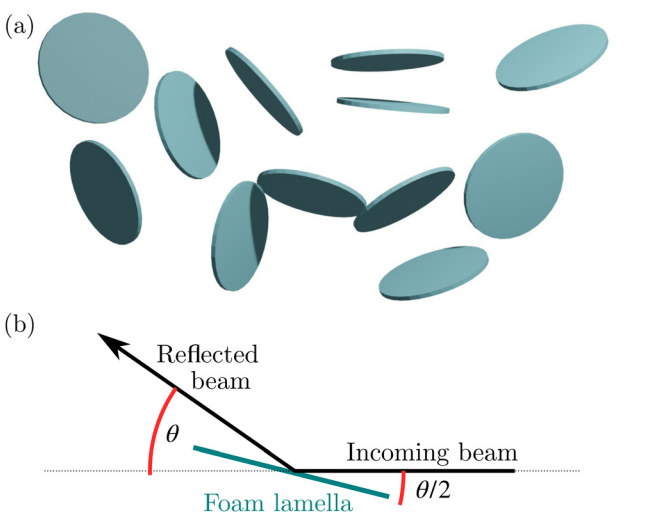

Fig. 4 (a) Schematic representation of a collection of randomly-oriented discs simulating the flat inter-bubble films. (b) Schematic representation of the reflectivity process at an angle θ from one disc satisfying the specular condition.

and air. The radius of the disk for the fit was set to $r = 0.1$ mm, ($q = 2\pi/r = 10^{-6}$ Å^{-1}). The macroscopic value of the lamellae size has therefore no impact on the data analysis for the measured q range ($q \in [5 \times 10^{-3}; 2 \times 10^{-1}]$ Å^{-1}). The lamellae number density $^1N_{tot}$ is related to the film specific surface area as:

$$^1N_{tot} = \frac{S/V|_{film}}{\pi r^2} \quad (8)$$

with $S/V|_{film}$ being the specific surface of the foam films. Accordingly, the only adjustable parameters are the specific foam film surface $S/V|_{film}$ and the foam film thickness h. This equation is obtained within the Born approximation,[64] *i.e.* the amplitude of the incident wave remains constant through the scattering object. This implies that the scattered or adsorbed intensity is negligible with respect to the transmitted one. While the Born approximation is at the basis of the vast majority of small-angle scattering analyses, this model is not able to describe our experimental data around 0.15 Å^{-1}, as shown in Fig. 5a with a pseudo plateau that is reinforced as the foam is drying. The oscillations and the plateau in the intensity curve cannot be described considering the scattering contribution of the lamellae in addition to the contribution of the Plateau borders and of the micelles, as shown in Fig. S4 in the ESI.† According to recent publications on foam small-angle scattering,[65] this plateau appears to correspond to the reflectivity plateau of an air/D_2O/air film of several nm thickness. We can consider that the large foam films give rise to a specular reflection signal, provided the specular condition – the incidence angle equals the reflection angle – is met, as shown in Fig. 4b. Thus, the Born approximation does not hold below the critical angle, where every neutron is reflected, and thus, the typical small-angle scattering formalism cannot be employed for taking into account the thin film scattering contribution.

Thus, in a second approach, we assume that the disks are large and flat, compared to the neutron coherence length, and so a specular reflection of the air/D_2O/air interface takes place. From the definition of the scattering intensity which relates the scattering cross section to the illuminated volume A_0T and solid angle $\Delta\Omega$, it follows that:[66]

$$I^{reflec}_{lamellae}(q) = R(q,h,\Delta\rho,\Sigma)A(\theta)\cdot\frac{1}{A_0T}\cdot\frac{1}{\Delta\Omega} \quad (9)$$

with $R(q,h,\Delta\rho,\Sigma)$ being the probability of a neutron being reflected at a given scattering vector, $A(\theta)$ the projected area of the foam on the beam-axis, A_0 the area of the neutron beam, T the sample thickness and $\Delta\Omega$ the solid angle. $R(q,h,\Delta\rho,\Sigma)$ is computed assuming a layered air–D_2O–air system with a thickness h, roughness Σ, with $\Delta\rho$ the difference in scattering length density of D_2O and air according to the recursive Parratt formalism.[67] The Parratt formalism allows to calculate the reflected intensity for a multilayered system using the Fresnel coefficients of each interface. Provided the very low roughness characterizing the foam films – induced by thermal fluctuations of the air/surfactant solution interface which is around $\Sigma \simeq \sqrt{k_BT/\gamma} = 0.3$ nm–, off-specular reflection can be safely neglected. The solid angle is given by:

$$\Delta\Omega = 2\pi\sin\theta\Delta\theta \quad (10)$$

The projected area of the foam on the beam-axis is given by:

$$A(\theta) = N_{spec}\pi r^2\sin(\theta/2) \quad (11)$$

with πr^2 being the area of one lamella, and N_{spec} the number of lamellae satisfying the specular condition. We assume that the lamellae are randomly oriented and thus the fraction of lamellae satisfying the specular condition depends on the beam divergence θ_{div} as:

$$N_{spec} = N_{tot}\frac{\theta_{div}}{\pi} \quad (12)$$

Substituting eqn (10)–(12) in eqn (9), one obtains:

$$I^{reflec}_{lamellae}(q) = R(q,h,\Delta\rho,\Sigma)\frac{N_{tot}\pi r^2(\theta_{div}/\pi)\sin(\theta/2)}{TA_0 2\pi\sin\theta\Delta\theta} \quad (13)$$

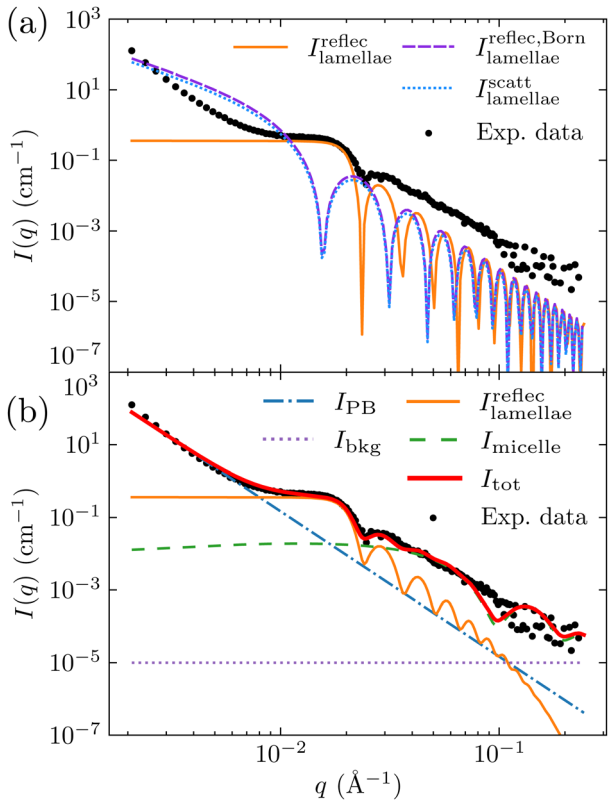

Fig. 5 (a) Foam scattering data collected at 65 min of aging to which are superimposed either scattering intensity from randomly-oriented discs (eqn (7), blue line) or reflectivity signal with (eqn (16), purple line) or without (eqn (15), orange line) the Born approximation from the same set of discs without taking into account a surface roughness. (b) Same data adjusted with a model at three contributions: I_{PB} from Plateau borders, $I_{micelle}$ from micelles present within the foam and $I^{reflec}_{lamellae}$ from discs considering the reflectivity assumption according to eqn (15) with a film roughness /polydispersity Σ = 1.5 nm. I_{bkg} is the incoherent scattering background.

which, in the small-angle approximation ($\sin(x) \approx x$), simplifies to:

$$I^{\text{reflec}}_{\text{lamellae}}(q) = R(q,h,\Delta\rho,\Sigma)\frac{{}^{1}N_{\text{tot}}r^2\theta_{\text{div}}}{4\pi\Delta\theta} \quad (14)$$

with ${}^{1}N_{\text{tot}} = N_{\text{tot}}/(TA_0)$ being the number of lamellae per scattering volume. If $\Delta\theta$, arising from the definition of the solid angle is approximated with the beam divergence, eqn (14) further simplifies to:

$$I^{\text{reflec}}_{\text{lamellae}}(q) = \frac{S}{V}\bigg|_{\text{film}}\frac{R(q,h,\Delta\rho,\Sigma)}{4\pi^2} \quad (15)$$

By adding the specific surface of the films $S/V|_{\text{film}}$ and the one from the Plateau Borders $S/V|_{\text{PB}}$, it is possible to estimate the total specific surface of the foam $S/V|_{\text{foam}} = S/V|_{\text{PB}} + S/V|_{\text{film}}$. This provides an elegant relationship between the measured scattering intensity, the reflectivity signal, and the foam area per unit volume. Accordingly, through eqn (9)–(15), a formalism to relate the reflection signal arising from the foam film in absolute units was derived. As shown in Fig. 5a, the intermediate range of the scattering data can be described using the "reflectivity" approach.

To confirm that the difference between the calculated "scattered" (eqn (7)) *vs.* "reflected" (eqn (15)) wave comes from the different formalism used to derive the two calculated curves, the reflectivity signal was also calculated within the Born approximation. For a thin film of thickness h of D_2O in air, the reflected intensity calculated within the Born approximation is given by:[68]

$$I^{\text{reflec,Born}}_{\text{lamellae}}(q) = \frac{1}{4\pi^2}\frac{S}{V}\bigg|_{\text{film}}\frac{16\pi^2}{q^4}(2\Delta\rho)^2\sin^2\left(\frac{qh}{2}\right) \quad (16)$$

The three calculated curves overlap at high-q (Fig. 5a), within the validity of the Born approximation, while they significantly differ at small angles. In particular, only the reflectivity signal without the Born approximation can correctly describe the pseudo plateau in scattering data. It is also noteworthy that the spacing between the minima differs according to the model used in the intermediate q region. In particular, the position of the first minimum in the reflectivity curve depends not only on the film thickness but also on the scattering length densities (SLD). This implies that the foam film thickness can be determined from the position of the oscillation only if three or more oscillations are present in the data or if the SLD profile of the film is taken into account in the analysis.

Fig. 5b shows the different contributions and the resulting intensity for a dry, 65 min-old foam, taking into account the Porod scattering from the Plateau borders, the reflection at the foam-film interface without Born approximation, and the scattering of the micellar aggregates presents in the foam channels. While several examples dealing with the analysis of SANS data from liquid foams can be found in the literature,[39–45,47,48] this is the first example of quantitative analysis, in absolute scale, of the scattering data recorded from liquid foams. The analysis was performed using a value for the film roughness Σ of 1.5 nm, which is much larger than the roughness due to thermal fluctuation of around 0.3 nm. A higher value for Σ was chosen since the films in the scattering volume are not fully monodisperse and it is, therefore, necessary to take into account the thickness polydispersity to analyze the scattering curves. The value of Σ is thus used to describe both the roughness and the polydispersity between the films and was arbitrarily set to 1.5 nm. However, the value represents a higher estimate for the film roughness, since the choice of smaller values down to 0.1 nm, has no impact on the fit quality and the obtained fit parameters, as demonstrated in Fig. S5 in the ESI.† There are only 4 parameters that are adjusted during the fit procedure: the liquid fraction ϕ, the film thickness h, and the specific surface area of the films $S/V|_{\text{film}}$ and of the Plateau borders $S/V|_{\text{PB}}$. The values obtained for the foam shown in Fig. 5b, at 65 min, are $\phi = (2.5 \pm 0.5)\%$, $h = (40 \pm 3)$ nm, $S/V|_{\text{PB}} = (6.1 \pm 0.1)$ cm^{-1} and $S/V|_{\text{film}} = (14.3 \pm 0.5)$ cm^{-1}. Such information is not available by any other technique.

4 Results and discussion

Hereafter, the stability of a nonionic/anionic surfactant stabilized foam is investigated by following foam volume using the foam analyzer, and by measuring bubble size distribution, specific surface areas, liquid fraction, and thickness of the film as a function of time using the multi-scale setup. The goal of this case study is to provide the reader with an overview of the information that can be extracted from this multi-method approach coupled with suitable data analysis.

4.1 Macrostructural characterization

The evolution of the foam volume is shown as a function of time in Fig. 6. Time zero is defined as the moment where the gas flow is stopped. Accordingly, at negative times the foam is created, and fills the column for approximately 4 min. In parallel, the volume of the sub-phase solution is decreasing (dotted red curve in Fig. 6). Once the gas flow is stopped, the foam then evolves through a free drainage process. During the first 10 min after foaming, the kinetic of drainage is fast and water trapped within the foam drains through the Plateau borders with a drainage front which shifts downwards at constant velocity.[34] The volume of the foam decreases and reaches an inflection point. The second stage of drainage then begins, characterized by a slower regime. It has to be noted here that the decrease in foam volume, associated with the drainage of the liquid solution, takes place at the bottom of the foam, and that the total volume of the system, {foam + liquid solution}, remains relatively constant in this phase. Once the excess solution has drained within the foam after 10 minutes, the second regime of drainage, much slower, begins. In this phase, the interlamellar interactions and capillary forces act against gravity. This stage is characterized by a pseudo-plateau in the foam volume variation, which ends, in the investigated system, at approx. 30 minutes. At this stage, the foam at the top of the column is very dry; the bubbles start to break and the foam gradually collapses.

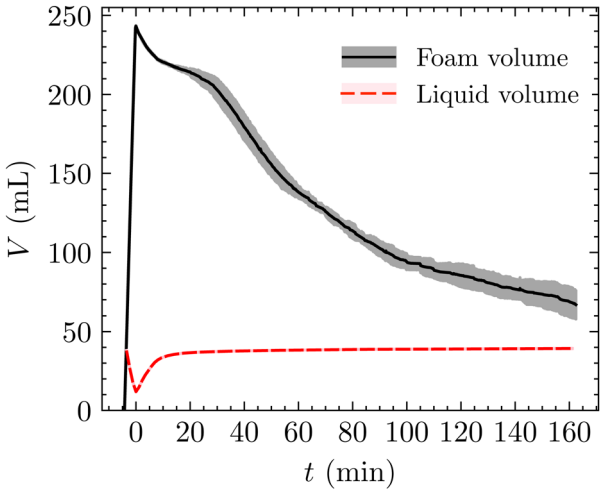

Fig. 6 Foam volume (black line) and solution at the bottom of the column (dotted red line) as a function of time. The respective standard deviations are plotted as the shaded region from three independent measurements using the Foam-analyzer. The liquid volume error bars are too small to be visible. Time t = 0 corresponds to the end of foaming.

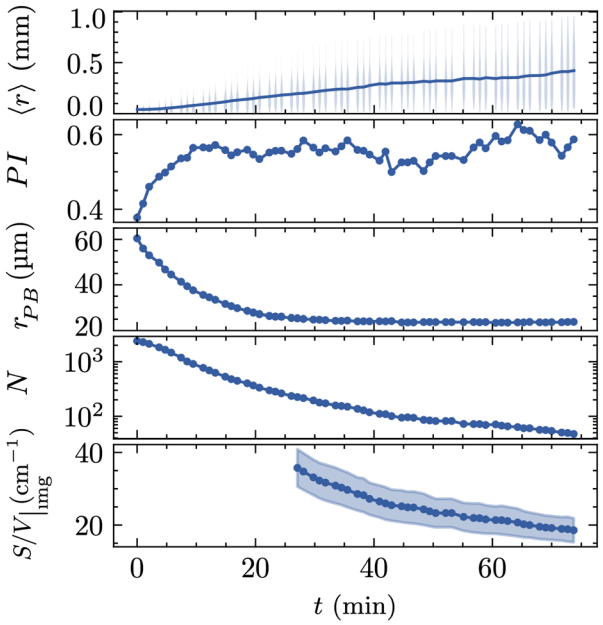

Fig. 7 Evolution of the average radius of the bubbles $\langle r \rangle$, of the polydispersity index PI, of the radius of the Plateau borders r_{PB}, of the number of bubbles N and of the total specific surface area of the foam $S/V|_{img}$ as a function of time, measured by the analysis of the images obtained during the SANS experiments. The probability density is plotted along the y axis as a "violin diagram". Error bars are represented as a shaded area. The model that determines the specific surface requires a very dry foam, which explains the absence of points below 20 min.

While the foam volume evolution provides a general overview of the foam stability, the simultaneous recording of foam photographs, electrical conductivity, and small-angle neutron scattering patterns allows us to get a deeper structural understanding of the foam aging mechanisms.

4.1.1 Bubble size distribution. Representative pictures of both a humid foam and a dry one are given in Fig. 3b and d, respectively, and all photos taken of the foam are shown in Fig. S6 in the ESI.† The mean size, polydispersity index of the foam bubbles, radius of the Plateau borders as well as the liquid fraction were analyzed according to the procedure described in Section 3.2 and the results of their time evolution are shown in Fig. 7.

The mean radius $\langle r \rangle$ increases from 0.04–0.43 mm with a slight inflection in its evolution around 40 min. The PI of the distribution increases quickly from 0.37–0.58 in the first 10 min to be then almost constant, whereas the number of bubbles N decreases continuously as a function of time. The radius of the Plateau borders decreases until reaching a plateau around 20 min. The increase in the radius of the bubbles over time as well as the decrease of N mean that coalescence and coarsening play a role in the decay of the foam as expected, but with kinetics that remain slow.

4.1.2 Liquid fraction. To obtain information about drainage, the time evolution of the liquid fraction ϕ was determined. As mentioned previously, four independent techniques were used: conductance measurements, image analysis, neutron beam transmission, and SANS data analysis. The data from the four techniques are given in Fig. 8a.

The SANS data give an overestimated value of ϕ compared to the other techniques which will be discussed in the Section 4.2. For the three other methods, although slight differences are visible, they are consistent and provide a clear trend for the evolution of the liquid volume fraction in the foam as a function of time. These three methods have different strengths and weaknesses to estimate the liquid volume fraction within the foam at a given height: electrical conductivity is a reliable and robust method when the system is rich in charge, but it can be applied to conductive solutions only; ϕ obtained from the image analysis suffers from the choice of the threshold during the binarisation procedure and is limited by the camera resolution. However, it can be applied to any foam, even non-ionic ones. Neutron transmission suffers from a low signal-to-noise ratio and although the measurements are taken primarily to obtain absolute units of the SANS data they are also used in this context to corroborate the correctness of the solution volume fraction at a given height in the foam and as a function of time. In our experiments, and in particular at high times (after 20 min), the measured conductance is low and close to the sensitivity limit of the conductivity meter (see Fig. 3e) which explains the large uncertainty of the liquid fraction. Despite different strengths and weaknesses, all three methods give similar results and make it possible to determine the time evolution type of the foam quality: wet foam ($\phi > 10\%$), dry foam ($\phi < 5\%$) or very dry foam ($\phi < 1\%$). The evolution of the liquid fraction determined by these three methods shows a bi-exponential decay:

$$\phi(t) = A\exp(-t/\tau_1) + B\exp(-t/\tau_2) \quad (17)$$

(see Fig. 8b). The characteristic times τ_1 and τ_2 obtained by the different methods are in good agreement around 5 min and 1 h

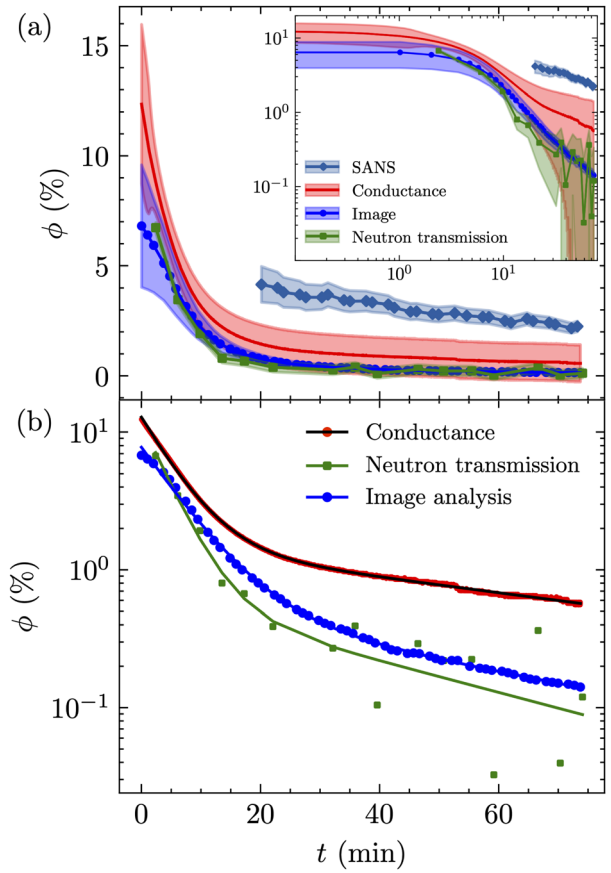

Fig. 8 (a) Determination of the liquid fraction ϕ at the height of prism 2 from mean conductance measurements on the electrode above and below the prism (red curve), from collected photo-images on the prism 2 (blue curve), from the transmission of the neutron beam (green curve), and from SANS analysis (light blue curve). The data are plotted on a log-log scale in the inset. Error bars are represented as shaded regions. (b) The same data (dots) are plotted on a log-linear scale and fitted using a bi-exponential decay represented by the lines (black, blue, and green).

Table 1 Characteristic decay times and their uncertainties for the liquid fraction time-variation according to the three techniques used

	τ_1 (min)	τ_2 (min)
Conductance	5 ± 1	77 ± 1
Neutron transmission	4 ± 2	40 ± 20
Image analysis	7 ± 1	51 ± 2

respectively and are given in Table 1. It is shown that the drying of the foam in this example takes place in two steps, a fast one with a characteristic time of a few minutes, followed by a slower one of approx. 1 hour.

4.2 Microstructural characterization of the foam

As detailed previously, SANS experiments were performed during foam aging to obtain microstructural information about the foam as a function of time. The SANS analysis model was applied to all the recorded scattering curves as shown in Fig. S7 in the ESI.† However, the SANS patterns of the young, wet foam (before 10 minutes), could not be fitted assuming specular reflection at the air/D_2O/air interface. At this stage, owing to the high liquid fraction (around 5%), the surfaces are too curved to provide a reflectivity signal. Between 10 and 20 min, the total reflectivity signal is visible in the experimental data. However, no Kiessig fringes, arising from the interference between the two interfaces of the film, are observed presumably due to the large film thickness or thickness polydispersity. Accordingly, the data between 10 and 20 min were fitted assuming a "thick" film of 60 nm. This dimension has, however, no real physical meaning. While the thickness of the foam films cannot be determined, this approach allows us to calculate the specific surface of the films from the intensity of the reflected signal below the total reflection angle q around 0.15 Å^{-1}. From 20 min onward, all structural parameters – the liquid fraction ϕ, the inter-bubble film thickness h, the specific surface areas from the Plateau borders $S/V|_{PB}$ and from the films $S/V|_{film}$ – can be obtained from the fit of the SANS data, and are shown in Fig. 9.

The liquid fraction obtained from the SANS analysis varies from 4 down to 2% in this time range. It appears to be overestimated compared to the values determined using conductance, neutron transmission, and image analysis. We recall that the liquid fraction from SANS was estimated assuming that concentration and shape of the surfactant micelles in the foam is equal to that in solution. The mismatch indicates that either the concentration of micelles in the foam is higher than in the bulk solution, or that the micellar aggregates are larger in the foam than in the solution. We refrain from further

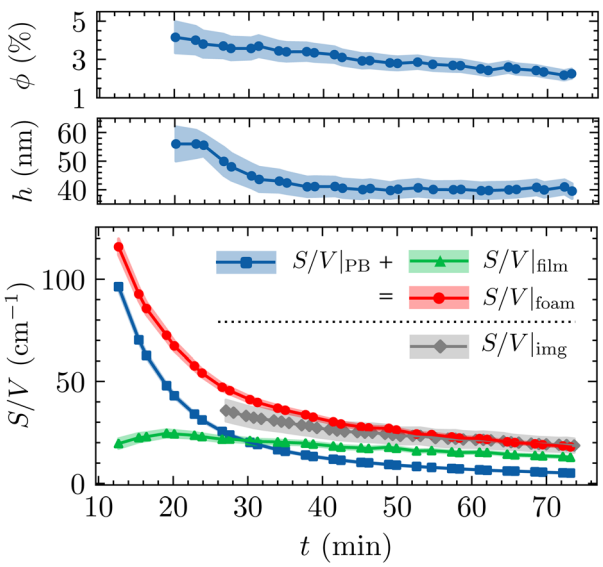

Fig. 9 Time evolution of the liquid fraction ϕ obtained from the small-angle scattering of the micelles (eqn (5)), the inter-bubble film thickness h and the specific surface S/V obtained from the reflectivity contribution from the thin films (eqn (15)). The total specific surface area of the foam $S/V|_{foam}$ is obtained by summing the surface area from the Plateau borders $S/V|_{PB}$ and from the films $S/V|_{film}$. Error bars are represented as shaded regions and are obtained by minimizing the residual error using the least squares method. The specific surface area obtained from image analysis $S/V|_{img}$ is also plotted for the sake of comparison.

investigating the variation of the shape/size/concentration of the micellar aggregates in the foam since, despite being a fundamentally interesting observation, it exceeds the scope of this work. We only hint that performing contrast variation experiments would allow probing the structure of colloidal assemblies within the foam with high accuracy. However, this overestimation of the liquid fraction is not prejudicial to the estimation of specific surface areas and film thickness. Indeed, the specific surface areas S/V are obtained from the q^{-4} decay for the PB and from the inflection point at the critical angle for the films. They are both well-defined, which explains the small errors on these parameters, and located in regions of the scattering pattern where the contribution of the micelles is negligible. For what concerns the foam film thickness h, it is determined from the position of the oscillations, which are found in the q range from 0.003 to 0.05 Å^{-1}. In this region, the contribution of the micelles is constant, despite being non-negligible. In other words, if an error is made in the contribution of the micelle scattering to the overall scattering intensity, this does not impact the reliability of the other values determined by the analysis of the SANS data. This is confirmed by the correlation coefficients between the four fit parameters which are very low and given in Table S3 of the ESI.† Besides, the specific surface area of the foam (represented in red in Fig. 9) obtained with SANS perfectly agrees with the one obtained from image analysis (represented in grey), ruling out systematic errors in the absolute scale of the SANS experiments.

As soon as the Kiessig fringes are observable, the foam film thickness decreases from about 55 nm down to 40 nm a value which remains constant over the last 30 min of the experiment. These values are in the range of what has been determined using a thin film pressure balance technique on a single film submitted to an external pressure before rupture, but still much thicker than Newton black films.[69] Finally, the last microscopic features are the specific areas from Plateau borders and foam films. Their sum agrees very well with the results from the image analysis, at least in the last 30 minutes, supporting the use of the absolute scale in the scattering experiment. In particular, the analysis of the SANS data allows us to discern directly between the two specific surface areas, $S/V|_{\mathrm{PB}}$ and $S/V|_{\mathrm{film}}$. While the surface area of the foam film decreases only moderately with time, the Plateau border area decreases significantly within the investigated time range, from 100 to less than 10 cm^{-1}. The Plateau borders specific surface area decreases with a bi-exponential law (see Fig. S8 in the ESI†), with characteristic times of (7 ± 1) and (42 ± 2) minutes. In contrast, the specific surface area of the films decreases slowly, mostly linearly in time. Thus, the sum is dominated by the Plateau borders contribution at the beginning of drainage and then by the foam film when the foam is aged and dried.

4.3 Calculation of the disjoining pressure

As soon as the foam is formed, in the example presented here, the liquid structure is immediately subjected to free drainage which will contribute to its destabilization. During the first drainage stage, water drains rapidly through the foam with a drainage front that moves down to reach the foam/solution interface within a characteristic time of approximately 5–10 min in this geometry and formulation. For times larger than this characteristic time, the entire foam structure relaxes into an aging phase in which gravity is not the only force acting on the liquid. This time phase corresponds to the pseudo plateau observed around 10 min in Fig. 6. The foam becomes dry with a liquid fraction $\phi < 5\%$. It is interesting to note that during the first 10 minutes, the PI of the radius of the bubble increases significantly to achieve a quasi-constant and large value of about 0.57. This second phase in the foam aging observed after 10 min, corresponds to a much slower process characterized by a set of bubbles that become faceted. The signature of this evolution can be followed by the fluctuations of the scattering intensity, which increase in number and amplitude, and start to be detectable on the 2D-detector (see Fig. S9 and S10 in the ESI†).[70] The bubble size variation first follows a quasi-proportional time law (proportional to t^{β} with $\beta < 1$) and then a trend close to $t^{1/2}$ at long time (see Fig. S11 in the ESI†), an evolution characteristic of a coarsening process.[71] The specific surface area of the foam decreases, mainly due to the decrease in the specific surface area of the Plateau borders contribution, until the one of the films becomes predominant. The film thickness decreases until a quasi-constant value. This value is tuned by a balance between the capillary pressure P_{c} and the sum of the disjoining pressure Π_{d}, that prevents further thinning of the film and ensures mechanical resistance to coalescence and to coarsening, and the hydrodynamic pressure ΔP due to capillary suction: $P_{\mathrm{c}} = \Pi_{\mathrm{d}} + \Delta P$.[72] Determining roughly the Plateau borders radius from image analysis, of about $r_{\mathrm{PB}} = 24$ μm at the end of the experiment and with the measurement of the surface tension in this system, equal to $\gamma = 32$ mN m^{-1}, it is possible to estimate the capillary pressure – defined for a dry foam[34] as $P_{\mathrm{c}} = \gamma/r_{\mathrm{PB}}$ – of about 1350 Pa. At that time, the film thickness is constant and the foam reaches an equilibrium state, thus the capillary pressure is equal to the disjoining pressure Π_{d}. For the younger foam, it is necessary to estimate the hydrodynamic pressure loss between the centre of a soap film and the neighbouring Plateau borders during capillary suction. Let v be the typical velocity of the liquid within the film, driven by capillary suction, and a_{film} the typical radius of the film, as represented in Fig. 10.

Then by Poiseuille law, the typical pressure drop across the film[73] is $\Delta P \approx \eta a_{\mathrm{film}} v/h^2$. It is possible to estimate the velocity v from the film thinning rate $\dot{h}$ considering the following mass balance:

$$\rho a_{\mathrm{film}} v h \approx \rho {a_{\mathrm{film}}}^2 \dot{h} \tag{18}$$

with $\rho a_{\mathrm{film}} v h$ the mass flow rate driven by capillary suction and $\rho {a_{\mathrm{film}}}^2 \dot{h}$ the mass flow rate during the thinning of the films. Therefore,

$$\Delta P \approx \eta {a_{\mathrm{film}}}^2 \dot{h}/h^3. \tag{19}$$

To get a numerical estimate, we take $\eta = 10^{-3}$ Pa s, and $h \approx$ 50 nm from Fig. 9. Since the bubble radius varies between 0.2 and 0.4 mm between 20 min and the end of the experiment, the order of magnitude of the film radius is $a_{\mathrm{film}} \approx 10^{-4}$ m.

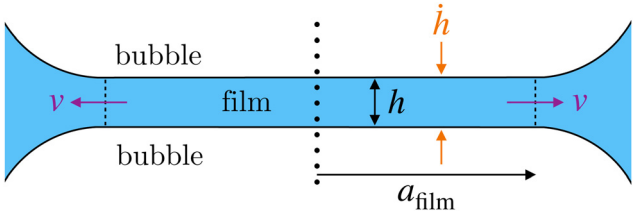

Fig. 10 Schematic representation of film thinning and capillary suction. v is the typical velocity of the fluid, a_{film} and h are the typical radius and thickness of the film, respectively, and $\dot{h}$ is the thinning rate of the film.

To estimate the thinning rate, the data from Fig. 9 suggest a variation of 20 nm over 20 min, hence $\dot{h} \approx 2 \times 10^{-11}$ m s^{-1}. Everything combined, we thus estimate $\Delta P \approx 2$ Pa. This pressure contribution remains between two and three orders of magnitude lower than the capillary pressure allowing us to neglect it, and so $P_c \approx \Pi_d$ even in the out-equilibrium condition. Fig. 11 thus presents the evolution of the disjoining pressure estimated from image analysis as a function of the film thickness obtained from SANS analysis at the same time. Pressure values regarding the film thickness are reasonable if it is compared to the values measured for SDS by varying the ionic strength.[74]

Two trends can be observed in Fig. 11. Between 22 and 42 min, the foam film thins while the disjoining pressure – approximated by the capillary pressure as the hydrodynamic contribution is negligible as discussed above – increases. The liquid fraction estimated by image analysis changes from (0.7 ± 0.2)% to (0.3 ± 0.1)%. Thus, the two interfaces of the film get closer to each other until the film reaches an equilibrium thickness h = 40 nm from 44 min onward. The films do not drain anymore and the equilibrium pressure is reached. It is interesting to notice that the thinning velocity is close to zero (slope of the thickness variation *versus* time, see Fig. 9) when the contribution of the films to the foam specific surface area becomes larger than that of the Plateau borders. Both the liquid content of the foam and the Plateau border specific area show a similar bi-exponential decay supporting the idea that the drainage of the solution takes place mainly through the Plateau borders.[75,76] After this transient period ending around 40 min, the foam aging enters a self-similar growth regime where the mean radius of bubble $\langle r \rangle$ evolves in $t^{1/2}$ (see Fig. S11 in the ESI†).

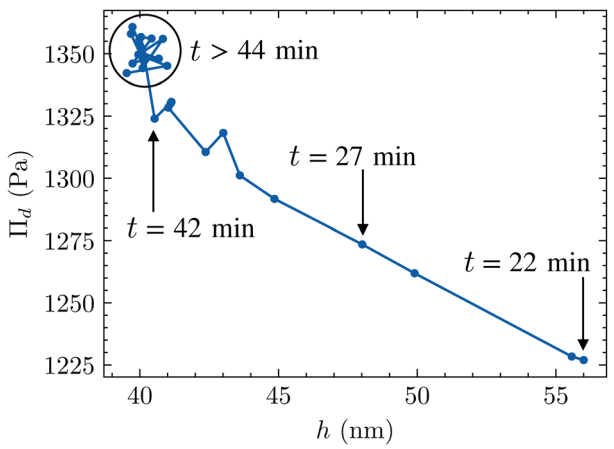

Fig. 11 Disjoining pressure Π_d calculated from the values of the Plateau borders radius as a function of the film thickness h obtained by SANS data analysis. Some specific moments were identified on the figure to make it easier to follow the process through time.

5 Conclusion

In summary, the analysis of foam stability requires the collection of a wide range of information from the nano- to the centimetre scale that has to be correlated for a better understanding of the underlying processes. While such a multi-scale analysis is mostly performed using different techniques separately in the literature,[34,77] herein the evolution of foam has been followed simultaneously using macro-photography, electrical conductivity, and small-angle neutron scattering. The combination of these three techniques allows us to perform this multi-scale analysis in real-time on a given sample. In particular, the analysis in absolute scale of the SANS data allows quantifying of the specific surface areas from Plateau borders and from inter-bubble thin films as well for which time their evolution can be correlated to the film thickness variation, while the analysis of the SANS data in arbitrary units only provided reliable values for the foam film thickness.[47,48]

To demonstrate the relevance of the method and the setup, the aging of a liquid foam stabilized by a non-ionic BrijO10 and anionic SDS surfactant mixture was studied. With this new device, we have been able to follow the evolution of the number of bubbles, and liquid fraction using three different methods, but also the thickness of the inter-bubble film as well as the specific surface of the foam. To the best of our knowledge, it is the first report of the structural characterization of a liquid foam which simultaneously covers six orders of magnitude in size, from the nanometer scale of the micelles to the millimeter scale of the foam bubbles. From the evolution of the parameters, it was found that the aging of the foam follows a bi-exponential decay. The initial fast drying of the foam is due to the free drainage of the liquid through the Plateau borders. This process takes approximately 5–7 minutes to be completed. The free drainage is followed by further drying of the foam, where the liquid drainage is slowed down by capillary forces and repulsion between the foam films. This second drainage phase takes one hour approximately to be completed and to observe a self-similar regime of bubble growth. A rapid collapse of the foam follows its full drying once a critical disjoining pressure is achieved, about 1350 Pa for the studied system. This is the first time that a relationship between the disjoining pressure Π_d in foams under free drainage (so in out-of-equilibrium conditions) and the foam film thickness h has been measured. These experiments are generally done on single films in a thin-film pressure balance. Moreover, the final disjoining pressure values obtained are relatively low compared to the maximum value of disjoining pressure measured at

rupture for the film alone[74] suggesting that the destabilization of the foam does not depend directly on disjoining pressure.

Getting such a detailed overview of the evolution of foam is a fundamental step to tailor the foam for specific needs. For instance, one of the strategies to obtain wet foams is to reduce drainage by adding thickeners.[78] The present approach allows us to relate the characteristic times of drainage with the thickener concentration, which enables to refine the properties of the foam. In more general terms, having access to the details of the destabilization mechanisms of liquid foams is the prerequisite for designing novel foams with the desired properties.

Author contributions

L. C., O. D. and J.-L. B. conceived the project. L. C. and O. D. supervised the project, J. L., L. C., O. D. and P. B. conducted the experiments. J. L. participated in the development of the device. J. L., B. D., and L. C. performed data analysis. J. L., L. C. and O. D. discussed the results. All authors commented on the work and reviewed the manuscript.

Conflicts of interest

The authors declare that they have no competing interests.

Acknowledgements

The Institut Laue-Langevin is acknowledged for providing beamtime on the small-angle scattering machines D22 and D33 (data available at: **https://doi.ill.fr/10.5291/ILL-DATA.9-10-1730**); the PSCM for providing the laboratory infrastructure where all off/line experiments were performed. Fruitful discussions with Sylvain Prevost, Charles Dewhurst, Frédéric Nallet, and Oleg Konovalov are heartily acknowledged. We thank Michel Bonnaud, Benoit Laurent and Abdelali Elaazzouzi for their help in the instrumental development. O. D. and P. B. acknowledge fundings from Agence Nationale de la recherche for FOAMEX project, grant number ANR17-CE008-0016.

Notes and references

1 C. Wang and H. A. Li, Stability and mobility of foam generated by gas-solvent/surfactant mixtures under reservoir conditions, *J. Nat. Gas Sci. Eng.*, 2016, **34**, 366–375.
2 M. H. Alooghareh, A. Kabipour, M. Ghazavi, S. Mohammad Mousavi Sisakht and M. Razavifar, Effects of different gases on the performance of foams stabilized by Cocamidopropyl betaine surfactant and silica nanoparticles: A comparative experimental study, *Petroleum*, 2021, DOI: **10.1016/j.petlm.2021.09.002**.
3 S. N. Tan, D. Fornasiero, R. Sedev and J. Ralston, The role of surfactant structure on foam behaviour, *Colloids Surf., A*, 2005, **263**, 233–238.
4 Z. Briceño-Ahumada and D. Langevin, On the influence of surfactant on the coarsening of aqueous foams, *Adv. Colloid Interface Sci.*, 2017, **244**, 124–131.
5 A.-L. Biance, A. Delbos and O. Pitois, How Topological Rearrangements and Liquid Fraction Control Liquid Foam Stability, *Phys. Rev. Lett.*, 2011, **106**, 068301.
6 A. Salonen, R. Lhermerout, E. Rio, D. Langevin and A. Saint-Jalmes, Dual gas and oil dispersions in water: production and stability of foamulsion, *Soft Matter*, 2012, **8**, 699–706.
7 E. Yoshida, R. Farajzadeh, S. Vincent-Bonnieu and N. Bourada Bourada, Effect of Gas Permeability and Solubility on Foam, *Soft Matter*, 2014, **2014**, 145352.
8 A. Saint-Jalmes, Physical chemistry in foam drainage and coarsening, *Soft Matter*, 2006, **2**, 836–849.
9 J. Boos, W. Drenckhan and C. Stubenrauch, Protocol for Studying Aqueous Foams Stabilized by Surfactant Mixtures, *J. Surfactants Deterg.*, 2013, **16**, 1–12.
10 V. V. Yaminsky, S. Ohnishi, E. A. Vogler and R. G. Horn, Stability of Aqueous Films between Bubbles. Part 1. The Effect of Speed on Bubble Coalescence in Purified Water and Simple Electrolyte Solutions, *Langmuir*, 2010, **26**, 8061–8074.
11 C. T. Nguyen, H. M. Gonnermann, Y. Chen, C. Huber, A. A. Maiorano, A. Gouldstone and J. Dufek, Film drainage and the lifetime of bubbles, *Geochem., Geophys., Geosyst.*, 2013, **14**, 3616–3631.
12 J. Miguet, F. Rouyer and E. Rio, The Life of a Surface Bubble, *Molecules*, 2021, **26**(5), 1317.
13 O. Arciniega Saavedra and J. Gracia Fadrique, Surface Tension and Foam Stability Prediction of Polydimethylsiloxane-Polyol Systems, *Open J. Phys. Chem.*, 2012, **2**, 189–194.
14 K. G. Marinova, E. S. Basheva, B. Nenova, M. Temelska, A. Y. Mirarefi, B. Campbell and I. B. Ivanov, Physico-chemical factors controlling the foamability and foam stability of milk proteins: Sodium caseinate and whey protein concentrates, *Food Hydrocolloids*, 2009, **23**, 1864–1876.
15 D. Georgieva, A. Cagna and D. Langevin, Link between surface elasticity and foam stability, *Soft Matter*, 2009, **5**, 2063–2071.
16 K. Małysa, R. Miller and K. Lunkenheimer, Relationship between foam stability and surface elasticity forces: Fatty acid solutions, *Colloids Surf.*, 1991, **53**, 47–62.
17 E. S. Benilov, C. P. Cummins and W. T. Lee, Why do bubbles in Guinness sink?, *Am. J. Phys.*, 2013, **81**, 88–91.
18 G. Liger-Belair and C. Cilindre, How Many CO2 Bubbles in a Glass of Beer?, *ACS Omega*, 2021, **6**, 9672–9679.
19 W. S. Y. Wong, A. Naga, L. Hauer, P. Baumli, H. Bauer, K. I. Hegner, M. D'Acunzi, A. Kaltbeitzel, H.-J. Butt and D. Vollmer, Super liquid repellent surfaces for anti-foaming and froth management, *Nat. Commun.*, 2021, **12**, 5358.
20 C. Hill and J. Eastoe, Foams: From nature to industry, *Adv. Colloid Interface Sci.*, 2017, **247**, 496–513.
21 C. Micheau, D. Dedovets, P. Bauduin, O. Diat and L. Girard, Nanoparticle foam flotation for caesium decontamination using a pH-sensitive surfactant, *Environ. Sci.: Nano*, 2019, **6**, 1576–1584.

22 B. S. Murray, Recent developments in food foams, *Curr. Opin. Colloid Interface Sci.*, 2020, **50**, 101394.
23 F. Elias, J. Crassous, C. Derec, B. Dollet, W. Drenckhan, C. Gay, V. Leroy, C. Noûs, J. Pierre and A. Saint-Jalmes, The Acoustics of Liquid Foams, *Curr. Opin. Colloid Interface Sci.*, 2020, **50**, 101391.
24 T. Majeed, M. S. Kamal, X. Zhou and T. Solling, A Review on Foam Stabilizers for Enhanced Oil Recovery, *Energy Fuels*, 2021, **35**, 101391.
25 P. Trinh, A. Mikhailovskaya, M. Zhang, P. Perrin, N. Pantoustier, G. Lefèvre and C. Monteux, Leaching Foams for Copper and Silver Dissolution: A Proof of Concept of a More Environmentally Friendly Process for the Recovery of Critical Metals, *ACS Sustainable Chem. Eng.*, 2021, **9**, 14022–14028.
26 J. Rakowska, Best practices for selection and application of firefighting foam, *MATEC Web Conf.*, 2018, **247**, 00014.
27 T. Schad, N. Preisig, D. Blunk, H. Piening, W. Drenckhan and C. Stubenrauch, Less is more: Unstable foams clean better than stable foams, *J. Colloid Interface Sci.*, 2021, **590**, 311–320.
28 C. Stubenrauch, M. Hamann, N. Preisig, V. Chauhan and R. Bordes, On how hydrogen bonds affect foam stability, *Adv. Colloid Interface Sci.*, 2017, **247**, 435–443.
29 R. Höhler, S. Cohen-Addad and D. J. Durian, Multiple light scattering as a probe of foams and emulsions, *Curr. Opin. Colloid Interface Sci.*, 2014, **19**, 242–252.
30 B. Dollet and C. Raufaste, Rheology of aqueous foams, *C. R. Phys.*, 2014, **15**, 731–747.
31 D. Langevin, Influence of interfacial rheology on foam and emulsion properties, *Adv. Colloid Interface Sci.*, 2000, **88**, 209–222.
32 S. A. Koehler, S. Hilgenfeldt and H. A. Stone, A Generalized View of Foam Drainage: Experiment and Theory, *Langmuir*, 2000, **16**, 6327–6341.
33 A. Saint-Jalmes, Physical chemistry in foam drainage and coarsening, *Soft Matter*, 2006, **2**, 836–849.
34 I. Cantat, C.-A. Sylvie, E. Florence, G. François, H. Reinhard, O. Pitois, R. Florence and A. Saint-Jalmes, *Foams: Structure and Dynamics*, Oxford University Press, 2013.
35 A.-L. Fameau, A. Saint-Jalmes, F. Cousin, B. Houinsou Houssou, B. Novales, L. Navailles, F. Nallet, C. Gaillard, F. Boué and J.-P. Douliez, Smart Foams: Switching Reversibly between Ultrastable and Unstable Foams, *Angew. Chem., Int. Ed.*, 2011, **50**, 8264–8269.
36 K. G. Marinova, E. S. Basheva, B. Nenova, M. Temelska, A. Y. Mirarefi, B. Campbell and I. B. Ivanov, Physico-chemical factors controlling the foamability and foam stability of milk proteins: Sodium caseinate and whey protein concentrates, *Food Hydrocolloids*, 2009, **23**, 1864–1876.
37 A. Sheludko, Thin liquid films, *Adv. Colloid Interface Sci.*, 1967, **1**, 391–464.
38 O. Velev, G. Constantinides, D. Avraam, A. Payatakes and R. Borwankar, Investigation of Thin Liquid Films of Small Diameters and High Capillary Pressures by a Miniaturized Cell, *J. Colloid Interface Sci.*, 1995, **175**, 68–76.
39 O. T. Mansour, B. Cattoz, M. Beaube, M. Montagnon, R. K. Heenan, R. Schweins, M.-S. Appavou and P. C. Griffiths, Assembly of small molecule surfactants at highly dynamic air–water interfaces, *Soft Matter*, 2017, **13**, 8807–8815.
40 S. Yada, H. Shimosegawa, H. Fujita, M. Yamada, Y. Matsue and T. Yoshimura, Microstructural Characterization of Foam Formed by a Hydroxy Group-Containing Amino Acid Surfactant Using Small-Angle Neutron Scattering, *Langmuir*, 2020, **36**, 7808–7813.
41 R. Poryles, T. Chevalier, N. Gland, E. Rosenberg and L. Barré, Characterization of foam flowing in a granular medium in the presence of oil by small angle neutron scattering, *Soft Matter*, 2020, **16**, 1771–1778.
42 C. Micheau, P. Bauduin, O. Diat and S. Faure, Specific Salt and pH Effects on Foam Film of a pH Sensitive Surfactant, *Langmuir*, 2013, **29**, 8472–8481.
43 L. Zhang, A. Mikhailovskaya, P. Yazhgur, F. Muller, F. Cousin, D. Langevin, N. Wang and A. Salonen, Precipitating Sodium Dodecyl Sulfate to Create Ultrastable and Stimulable Foams, *Angew. Chem., Int. Ed.*, 2015, **54**, 9533–9536.
44 J. Hurcom, A. Paul, R. K. Heenan, A. Davies, N. Woodman, R. Schweins and P. C. Griffiths, The interfacial structure of polymeric surfactant stabilised air-in-water foams, *Soft Matter*, 2014, **10**, 3003–3008.
45 I. Schmidt, B. Novales, F. Boué and M. Axelos, Foaming properties of protein/pectin electrostatic complexes and foam structure at nanoscale, *J. Colloid Interface Sci.*, 2010, **345**, 316–324.
46 S. Perticaroli, J. Herzberger, Y. Sun, J. D. Nickels, R. P. Murphy, K. Weigandt and P. J. Ray, Multiscale Microstructure, Composition, and Stability of Surfactant/Polymer Foams, *Langmuir*, 2020, **36**, 14763–14771.
47 M. Hohenschutz, I. Grillo, C. Dewhurst, P. Schmid, L. Girard, A. Jonchère, O. Diat and P. Bauduin, Superchaotropic nano-ions as foam stabilizers, *J. Colloid Interface Sci.*, 2021, **603**, 141–147.
48 M. Kühnhammer, L. Braun, M. Ludwig, O. Soltwedel, L. Chiappisi and R. von Klitzing, A new model to describe small-angle neutron scattering from foams, *J. Appl. Crystallogr.*, 2022, **55**, 758–768.
49 M. A. V. Axelos and F. Boué, Foams As Viewed by Small-Angle Neutron Scattering, *Langmuir*, 2003, **19**, 6598–6604.
50 T. Widmann, L. P. Kreuzer, M. Kühnhammer, A. J. Schmid, L. Wiehemeier, S. Jaksch, H. Frielinghaus, O. Löhmann, H. Schneider, A. Hiess, R. von Klitzing, T. Hellweg and P. Müller-Buschbaum, Flexible Sample Environment for the Investigation of Soft Matter at the European Spallation Source: Part II—The GISANS Setup, *Appl. Sci.*, 2021, **11**(9), 4036.
51 F. Liu, Z. Wang, D. Sun, X. Wei, W. Zhou, G. Li and G. Zhang, Adsorption Kinetics of Brij 97 at the Air/Solution Interface, *J. Dispersion Sci. Technol.*, 2006, **27**, 657–663.
52 B. Petkova, S. Tcholakova, M. Chenkova, K. Golemanov, N. Denkov, D. Thorley and S. Stoyanov, Foamability of aqueous solutions: Role of surfactant type and concentration, *Adv. Colloid Interface Sci.*, 2020, **276**, 102084.

53 S. Mukherjee and H. Wiedersich, Morphological and viscoelastic properties of dense foams generated from skin cleansing bars, *Colloids Surf., A*, 1995, **95**, 159–172.
54 C. D. Dewhurst, I. Grillo, D. Honecker, M. Bonnaud, M. Jacques, C. Amrouni, A. Perillo-Marcone, G. Manzin and R. Cubitt, The small-angle neutron scattering instrument D33 at the Institut Laue-Langevin, *J. Appl. Crystallogr.*, 2016, **49**, 1–14.
55 ILL, GRASP, **https://www.ill.eu/users/support-labs-infrastructure/software-scientific-tools/grasp**, [Online; accessed 22-July-2022].
56 G. Bradski, The OpenCV Library, Dr Dobb's Journal of Software Tools, 2000.
57 Y. Wang and S. J. Neethling, The relationship between the surface and internal structure of dry foam, *Colloids Surf., A*, 2009, **339**, 73–81.
58 E. Forel, E. Rio, M. Schneider, S. Beguin, D. Weaire, S. Hutzler and W. Drenckhan, The surface tells it all: relationship between volume and surface fraction of liquid dispersions, *Soft Matter*, 2016, **12**, 8025–8029.
59 K. Feitosa, S. Marze, A. Saint-Jalmes and D. J. Durian, Electrical conductivity of dispersions: from dry foams to dilute suspensions, *J. Phys.: Condens. Matter*, 2005, **17**, 6301–6305.
60 NIST, Neutron Activation and Scattering Calculator, **https://www.ncnr.nist.gov/resources/activation**, [Online; accessed 22-July-2022].
61 G. Porod, *Small angle X-ray scattering*, Academic Press, New York, 1982, pp. 17–51.
62 W. Drenckhan and S. Hutzler, Structure and energy of liquid foams, *Adv. Colloid Interface Sci.*, 2015, **224**, 1–16.
63 J. S. Pedersen, *Neutrons, X-rays and Light: Scattering Methods Applied to Soft Condensed Matter*, Elsevier Science BV, 2002, pp. 391–420.
64 M. Born, Quantenmechanik der Stoßvorgänge, *Z. Phys.*, 1926, **38**, 803–827.
65 A. Mikhailovskaya, L. Zhang, F. Cousin, F. Boué, P. Yazhgur, F. Muller, C. Gay and A. Salonen, Probing foam with neutrons, *Adv. Colloid Interface Sci.*, 2017, **247**, 444–453.
66 *Neutrons, X-rays and Light: Scattering Methods Applied to Soft Condensed Matter*, ed. P. Lindner and T. Zemb, Elsevier Science Bv, Amsterdam, 2002, p. 444.
67 L. G. Parratt, Surface Studies of Solids by Total Reflection of X-Rays, *Phys. Rev.*, 1954, **95**, 359–369.
68 J. Penfold and R. K. Thomas, Neutron reflectivity and small angle neutron scattering: An introduction and perspective on recent progress, *Curr. Opin. Colloid Interface Sci.*, 2014, **19**, 198–206.
69 A. Mikhailovskaya, E. Chatzigiannakis, D. Renggli, J. Vermant and C. Monteux, From Individual Liquid Films to Macroscopic Foam Dynamics: A Comparison between Polymers and a Nonionic Surfactant, *Langmuir*, 2022, **38**, 10768–10780.
70 J. Etrillard, M. A. V. Axelos, I. Cantat, F. Artzner, A. Renault, T. Weiss, R. Delannay and F. Boué, In Situ Investigations on Organic Foam Films Using Neutron and Synchrotron Radiation, *Langmuir*, 2005, **21**, 2229–2234.
71 B. S. Gardiner, B. Z. Dlugogorski and G. J. Jameson, Coarsening of two- and three-dimensional wet polydisperse foams, *Philos. Mag. A*, 2000, **80**, 981–1000.
72 R. G. Horn, M. Asadullah and J. N. Connor, Thin Film Drainage: Hydrodynamic and Disjoining Pressures Determined from Experimental Measurements of the Shape of a Fluid Drop Approaching a Solid Wall, *Langmuir*, 2006, **22**, 2610–2619.
73 E. Chatzigiannakis, N. Jaensson and J. Vermant, Thin liquid films: Where hydrodynamics, capillarity, surface stresses and intermolecular forces meet, *Curr. Opin. Colloid Interface Sci.*, 2021, **53**, 101441.
74 N. Schelero, G. Hedicke, P. Linse and R. von Klitzing, Effects of Counterions and Co-ions on Foam Films Stabilized by Anionic Dodecyl Sulfate, *J. Phys. Chem. B*, 2010, **114**, 15523–15529.
75 R. A. Leonard and R. Lemlich, A study of interstitial liquid flow in foam. Part I. Theoretical model and application to foam fractionation, *AIChE J.*, 1965, **11**, 18–25.
76 O. Pitois, E. Lorenceau, N. Louvet and F. Rouyer, Specific Surface Area Model for Foam Permeability, *Langmuir*, 2009, **25**, 97–100.
77 C. Ochoa, S. Gao, S. Srivastava and V. Sharma, Foam film stratification studies probe intermicellar interactions, *Proc. Natl. Acad. Sci. U. S. A.*, 2021, **118**, 8915–8924.
78 H. Wang, X. Wei, Y. Du and D. Wang, Effect of water-soluble polymers on the performance of dust-suppression foams: Wettability, surface viscosity and stability, *Colloids Surf., A*, 2019, **568**, 92–98.